



Cite this: DOI: 10.1039/d3bm00837a

A facile one-stone-two-birds strategy for fabricating multifunctional 3D nanofibrous scaffolds

Altangerel Amarjargal,^{ID} *^{a,b} Zahra Moazzami Goudarzi,^a Olga Cegielska,^{ID} ^a
Arkadiusz Gradys,^{ID} ^a Dorota Kolbuk,^{ID} ^a Bartłomiej Kalaska,^{ID} ^c
Anna Ruszczyńska,^{ID} ^d and Pawel Sajkiewicz,^{ID} *^a

Local bacterial infections lead to delayed wound healing and in extreme cases, such as diabetic foot ulcers, to non-healing due to the impaired cellular function in such wounds. Thus, many scientists have focused on developing advanced therapeutic platforms to treat infections and promote cellular proliferation and angiogenesis. This study presents a facile approach for designing nanofibrous scaffolds in three dimensions (3D) with enhanced antibacterial activity to meet the need of treating chronic diabetic wounds. Being a cationic surfactant as well as an antimicrobial agent, octenidine (OCT) makes a 2D membrane hydrophilic, enabling it to be modified into a 3D scaffold in a "one stone, two birds" manner. Aqueous sodium borohydride (NaBH₄) solution plays a dual role in the fabrication process, functioning as both a reducing agent for the *in situ* synthesis of silver nanoparticles (Ag NPs) anchored on the nanofiber surface and a hydrogen gas producer for expanding the 2D membranes into fully formed 3D nanofiber scaffolds, as demonstrated by morphological analyses. Various techniques were used to characterize the developed scaffold (e.g., SEM, XRD, DSC, FTIR, and surface wettability), demonstrating a multilayered porous structure and superhydrophilic properties besides showing sustained and prolonged release of OCT (61% ± 1.97 in 144 h). Thanks to the synergistic effect of OCT and Ag NPs, the antibacterial performance of the 3D scaffold was significantly higher than that of the 2D membrane. Moreover, cell viability was studied *in vitro* on mouse fibroblasts L929, and the noncytotoxic character of the 3D scaffold was confirmed. Overall, it is shown that the obtained multifunctional 3D scaffold is an excellent candidate for diabetic wound healing and skin repair.

Received 15th May 2023

Accepted 7th June 2023

DOI: 10.1039/d3bm00837a

rsc.li/biomaterials-science

Introduction

Electrospinning is an effective technique for producing micro to nanofibers that has gained considerable attention in different sub-areas of nanomedicine, including biosensing, drug delivery, and tissue engineering.^{1–3} Due to their structural similarity to the tissue extracellular matrix (ECM) and the large specific surface area, nanofibrous membranes allow the fabrication of multifunctional and tailor-made drug delivery systems for tissue regeneration.^{4,5} For instance, Zhu *et al.* fab-

ricated an efficient electrospun membrane for wound healing that could guide and promote vascular regeneration *via* its aligned fibers and by sustained release of the tazarotene drug.⁶ However, such a kind of scaffold possesses a two-dimensional (2D) structure consisting of tightly packed fiber layers with only superficial pores because, in the electrospinning process, subsequent fiber layers are accumulated one on top of the other.^{7,8} This unavoidable characteristic hinders cell migration and growth throughout the nanofiber scaffolds and thus prevents proper tissue regeneration and integration.^{9,10} Therefore, tissue-engineered scaffolds should have a three-dimensional (3D) structure with loosely packed fiber layers to better mimic the native ECM and provide adequate space for cell migration and attachment.^{10,11}

Recently, significant efforts have been made to fabricate 3D nanofibrous scaffolds through the advancement of electrospinning technology, such as template-assisted, layer-by-layer, and self-assembly methods.^{12–15} These methods are mainly based on modifying the architecture of fiber collectors or incorporating sacrificial fractions. They show an advantage in

^aInstitute of Fundamental Technological Research, Polish Academy of Sciences, Pawińskiego 5b, 02-106 Warsaw, Poland. E-mail: psajk@ippt.pan.pl

^bPower Engineering School, Mongolian University of Science and Technology, 8th khoroo, Baga toiruu, Sukhbaatar district, Ulaanbaatar 14191, Mongolia. E-mail: amaraa1@must.edu.mn

^cDepartment of Pharmacodynamics, Medical University of Białystok, Mickiewicza 2c, 15-089 Białystok, Poland

^dFaculty of Chemistry, Biological and Chemical Research Centre, University of Warsaw, Zwirki I Wigury 101, 02-089 Warszawa, Poland

directly fabricating 3D porous scaffolds over classical electrospinning. Unfortunately, they are often ineffective and repetitive. Alternatively, post-processing 2D nanofibrous membranes by foaming is a common way to produce porous and thicker structures in the third dimension that can promote cellular infiltration and provide a better mimic for both the structure and composition of targeted tissues.^{16–18} Gas foaming processes use the nucleation and growth of gas bubbles *in situ* either *via* a chemical reaction or by adding inert gases into the polymer phase in different physical environments.¹⁹ Regarding the advantages of sodium borohydride (NaBH₄), it mediates the gas foaming method that converts 2D nanofibrous membranes to fabricate 3D scaffolds.^{20–22} Joshi *et al.* studied the hydrolysis reaction of sodium borohydride concerning the generation of hydrogen gas *in situ* in the pores, and they proposed the following reaction as the mechanism of rearranging the fibers into a 3D architecture.¹⁶



Various inorganic metal nanoparticles can be synthesized by *in situ* reduction of inorganic and organometallic precursors with sodium borohydride, which is the other benefit of this reducing agent.^{23–25} From this point of view, post-processing 2D nanofibers *via* a common key agent in both the gas foaming and NP synthesis reactions is a versatile technique to simultaneously realize multifunctional nanofibers in a loosely packed, 3-D architecture and their decoration with inorganic NPs. This can give electrospun nanofibrous membranes a broad set of new properties in addition to their main characteristics, such as a large surface-to-volume ratio and high encapsulation efficiency.^{26,27} Two separate studies have been reported on the preparation of silver nanoparticle-decorated²⁸ or drug-encapsulated 3D nanofiber scaffolds¹⁷ to enhance their functional performance; however, neither of these studies have fabricated *in situ* Ag NP decorated electrospun 3D nanofiber scaffolds able to encapsulate a therapeutic agent as a potential controlled drug release system with synergistic antibacterial properties. To the best of the authors' knowledge, no one has yet reported on the fabrication of drug-eluting 3D nanofiber scaffolds *in situ* decorated with Ag nanoparticles to develop antibacterial tissue scaffolds or wound dressing. This novel, so-called “one-stone-two-birds” strategy towards multifunctional 3D scaffolds will bring advantages to scaffolds by (i) generating a multilayered porous structure, (ii) co-loading antimicrobial agents in/on nanofibers and controlled release of the drug, and (iii) expanding the applications of 3D nanofiber scaffolds.

Since the encapsulated drug should not be released from the polymer matrices during fabrication, specially formulated nonwoven nanofiber membranes will be required. We expect that a 2D nanofiber system, inspired by our proof-of-concept study^{29,30} on controlled drug delivery through glass transition switching, can be an ideal membrane to prevent the premature release of loaded drugs at room temperature.

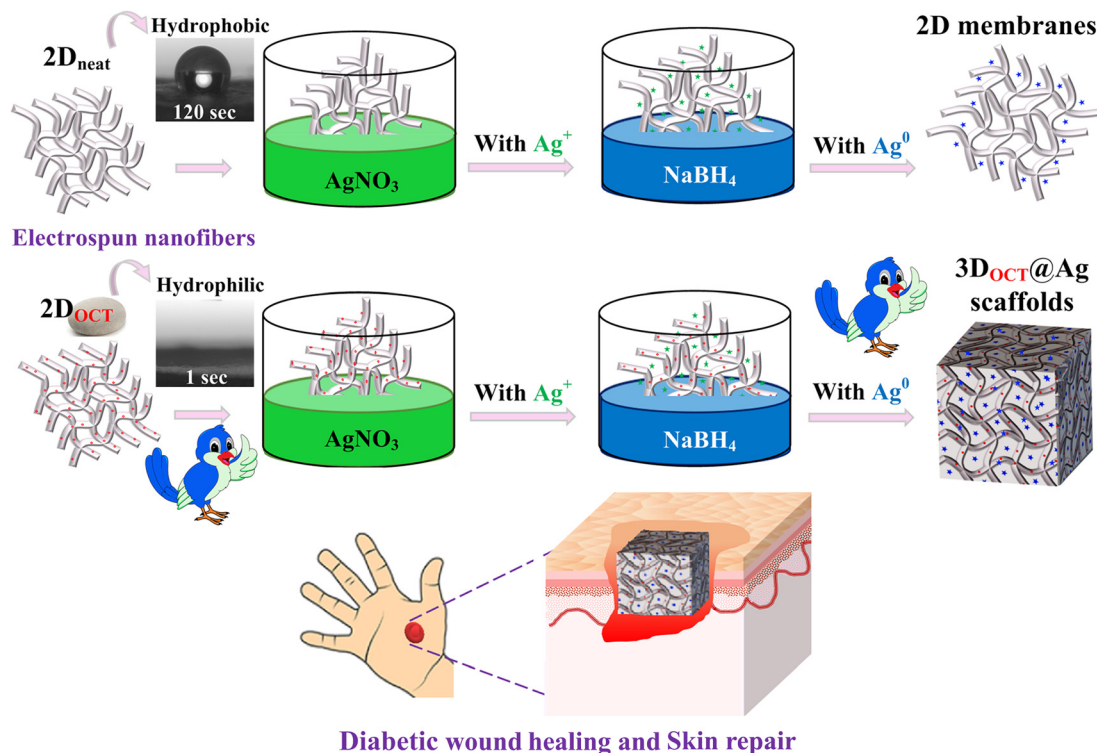
To verify our hypothesis, we first fabricated a drug-loaded electrospun nanofibrous membrane that can respond to the temperature change from 25 °C (room) to 37 °C (physiological) to regulate the release of encapsulated drugs. Sodium borohydride was then utilized as the immersion medium that can simultaneously lead to the *in situ* synthesis of Ag NPs anchored on the surface of support nanofibers and structural change of such a membrane, *i.e.*, Ag nanoparticles and 3D nanofiber scaffolds (Scheme 1). Our innovative technique for producing a multifunctional 3D scaffold addresses the limitations associated with 2D nanofibrous membranes, including their hydrophobic nature and the lack of bioactivity stemming from OCT encapsulation. In addition, the uniform dispersion of Ag NPs throughout the polymeric matrix imparts antibacterial properties to the scaffolds. As a result, the developed 3D scaffolds are anticipated to facilitate the healing of diabetic wounds and promote skin regeneration.

Materials and methods

All the chemicals were of analytical purity and used without any further purification. Poly(methyl methacrylate) (PMMA, $M_w = 100\,000 \text{ g mol}^{-1}$) was purchased from Polyscience. A copolymer of ethyl acrylate, methyl methacrylate, and with a low content of methacrylic acid ester of quaternary ammonium groups, Eudragit® RS 100 (ERS, $M_w = 32\,000 \text{ g mol}^{-1}$),³¹ was a gift sample from Evonik GmbH (Darmstadt, Germany). 1,1,1,3,3,3, -hexafluoro-2-propanol (HFIP) *N,N*-Dimethylformamide (DMF, 99.5%), and tetrahydrofuran (THF, 99.5%) were purchased from VWR International. Octenidine dihydrochloride (OCT) and silver nitrate (AgNO₃; $M_w = 169.87 \text{ g mol}^{-1}$) were purchased from Appollo Scientific (Cheshire, UK). Sodium bromide (NaBH₄) was purchased from Pol-Aura (Warsaw, Poland). Phosphate-buffered saline (PBS) was obtained from Sigma Aldrich. Lysogeny broth (LB) and lysogeny agar (LB agar) were purchased from A&A Biotechnology (Gdańsk, Poland), and Mueller-Hinton broth (MHB) was purchased from Pol-Aura (Warsaw, Poland). Bacteriological agar was purchased from BTL (Warsaw, Poland). Gram-negative bacterium *Escherichia coli* (*E. coli*) DH5α was obtained from the Laboratory of Calcium Binding Protein, Nencki Institute of Experimental Biology PAS (Warsaw, Poland). Gram-positive bacterium *Staphylococcus aureus* (*S. aureus*) ATCC 6538 was purchased from Argenta (Poznań, Poland).

Electrospinning of neat and OCT-loaded nanofibrous membranes

In a typical experiment, two separate solutions were intended for blend electrospinning: ERS (40 wt%) and PMMA (30 wt%) prepared by dissolving appropriate amounts in DMF and a binary solvent system of DMF–THF (9 : 1), respectively. The PMMA/ERS blend solution at 60/40 weight ratios was prepared by mixing calculated parts of the above solutions. The neat blend solution was kept stirring for 2 hours. In drug-loaded nanofibrous membranes, OCT was loaded by dissolution (3 wt% with respect to polymer amount) in HFIP and sub-



Scheme 1 Schematic illustration for the fabrication of multifunctional 3D nanofibrous scaffolds via the one-stone-two-birds strategy and application of 3D_{OCT}@Ag.

sequently added to the neat blend solution 2 hours before electrospinning. The solutions were loaded into a 10 mL syringe fitted with a metallic needle (21G) and electrospun using a Fluidnatek LE-50 (Bioinicia, Valencia, Spain) apparatus. The applied voltage and tip-to-collector distance were 18 kV and 15 cm during the spinning process, while the flow rate was kept at 1 mL h⁻¹. After electrospinning, the PMMA/ERS nanofiber mats were vacuum-dried in an oven at 25 °C for 24 h to remove the residual solvent.

One-pot fabrication of drug-eluting 3D nanofiber scaffolds decorated with Ag NPs

The drug-eluting nanofibrous scaffolds decorated with Ag NPs and their 3D formation were fabricated by *in situ* reduction and gas foaming techniques. Drug-loaded 2D nanofibrous mats (3.5 cm × 3.5 cm) were immersed in 20 mL of previously prepared aqueous AgNO₃ solution (10 mM) at room temperature for 10 minutes. Then, membrane samples were transferred to 30 mL of aqueous NaBH₄ (100 mM) solution to complete gas foaming and provide *in situ* reductions of Ag NPs. After 10 minutes of immersion, all samples were taken out, thoroughly rinsed with deionized water, and dried in a vacuum oven at 25 °C for 72 h. In this manuscript, 2D_{neat} and 2D_{OCT} refer to neat and drug-loaded nanofibrous membranes, while 3D_{OCT}@Ag refers to drug-eluting 3D nanofiber scaffolds decorated with Ag NPs.

Characterization

Scanning electron microscopy. The morphology of nanofibrous structures was studied by scanning electron microscopy (SEM, Jeol JSM-6010PLUS/LV InTouchScope™). Before starting SEM imaging, samples were sputter-coated with gold to increase the signal-to-noise ratio during the imaging process. The acceleration voltage was in the range of 7–10 kV.

Wide-angle X-ray scattering. Phase analysis and the study of crystallinity of samples were performed by wide-angle X-ray scattering (WAXS). Measurements were performed using a Bruker D8 Discover diffractometer operated at the voltage of 40 kV, current of 20 mA, and CuK_α radiation with a wavelength of 0.1542 nm. All measurements were carried out in reflection mode at room temperature.

Differential scanning calorimetry. A power compensated differential scanning calorimeter, Pyris1 DSC (PerkinElmer), equipped with Intercooler 2P, temperature, and heat calibrated using indium, zinc, and M24 standards, was used to measure the heat flow in the heating-cooling-heating mode. The temperature range was from -10 to 210 °C at the rate of 10 K min⁻¹ at nitrogen purge using samples weighing 4–7 mg. Each composition was measured using at least five samples for statistics.

Fourier transform infrared spectroscopy. Chemical bonds were analyzed by Fourier transform infrared (FTIR) spectroscopy. The samples were analyzed using VERTEX 70 (Bruker) in the range between 400 and 4000 cm⁻¹. A red laser

with 16 accumulations for each measurement at a laser power was used for scanning. Besides, each electrospun fiber sample and powder of OCT was measured three times, and similar results were obtained.

Surface wettability. Regarding surface wettability, contact angle measurement was conducted using Data Physics OCA 15EC (Germany). The water contact angle was measured three times on each sample. The samples were placed on a microscope glass slide, and 1 μL of water droplet was applied to each sample at room temperature; the surface wettability was measured at different times.

Drug loading and encapsulation efficiency of electrospun nanofibers

The OCT-loaded 2D membrane and 3D scaffold were carefully weighed and dissolved in DMF for 10 min using a magnetic stirrer ($n = 3$). The amount of drug in the respective solutions was calculated using a UV-visible microplate spectrophotometer (Multiskan Go, Thermo Fisher Scientific, USA) at a wavelength of 280 nm. The same solvent mixtures were used as blanks. The following equations were used to estimate the drug loading content (DLC) and drug encapsulation efficiency (DEE).³²

$$\text{DLC}(\%) = \frac{\text{(mass of the drug entrapped in the nanofibers)}}{\text{(mass of the nanofibers)} \times 100} \quad (2)$$

$$\text{DEE}(\%) = \frac{\text{(mass of the drug entrapped in the nanofibers)}}{\text{(mass of the drug added)} \times 100} \quad (3)$$

In vitro drug release tests

The release profile studies of OCT from the 2D membrane and 3D scaffold were performed in PBS buffer with pH 7.4 at different temperatures (32 $^{\circ}\text{C}$ and 37 $^{\circ}\text{C}$) and shaken at 50 rpm. A similar drug release test was carried out at 25 $^{\circ}\text{C}$ to see the effect of the temperature on OCT release behavior since the post-processing of 2D nanofibrous membrane by foaming occurred at room temperature. The samples were cut into pieces with the same mass of 10.0 mg and then immersed in 15 mL of buffer. At each immersion time, ranging from 0 to 144 h, 0.5 mL of sample was withdrawn and replaced with fresh medium to maintain the release conditions. The release of OCT from the samples was monitored with a UV-visible microplate spectrophotometer as described in the section “Drug loading and encapsulation efficiency of electrospun nanofibers”. The corresponding cumulative percentage of OCT released was determined using this wavelength’s pre-determined standard calibration curve.

Ag contents and Ag release kinetics

An inductively coupled plasma-mass spectrometer (ICP-MS, Nexion 300D, PerkinElmer, USA), equipped with a quartz cyclonic spray chamber, Meinhard nebulizer, and platinum cones, was employed to determine Ag contents and Ag release kinetics of the 3D_{OCT}@Ag sample. Quantitation was achieved

using a 4-point external calibration with a concentration range from 5 $\mu\text{g L}^{-1}$ to 200 $\mu\text{g L}^{-1}$. For the determination of the total content of Ag, a sample (0.014 g) was immersed in 45 mL of 65% HNO_3 for 24 h, then the solution was sampled, diluted, and analyzed in triplicate using ICP-MS. A blank sample consisting of 65% HNO_3 was prepared under the same conditions. To analyze the Ag release profiles, 0.020 g of the sample was immersed in 30 mL of deionized water under 300 rpm shaking conditions. A blank sample consisting of 30 mL of deionized water was subjected to the same treatment at the same time. An extract of 50 μL was collected every 2 hours for the first 12 hours and then once a day for the next 6 days. The extracts were diluted with 3% HNO_3 , and an ICP-MS analysis was performed in triplicate for each solution. The relative standard deviation did not exceed 5.0%.

Antibacterial assessments

Bacterial culture. *E. coli* (DH5 α) and *S. aureus* (ATCC 6538) were cultured on lysogeny broth (LB) agar and isolated by a streak plate method. An isolated colony was inoculated in 3 mL of fresh LB broth for a test and grown overnight at 37 $^{\circ}\text{C}$ in an orbital shaker.

Disc diffusion assay. Material samples were cut into 9 mm diameter circles and sterilized under UV light on both sides for one hour (30 min per sample side) to reduce the bioburden.³³ The concentration of overnight bacterial cultures of *E. coli* and *S. aureus* in LB broth was adjusted with fresh MHB to around 10^8 CFU mL^{-1} (approximately 0.5 McFarland Standard). The suspensions were then spread onto the surface of Mueller–Hinton agar (MHA) plates with sterile swabs by streaking each swab four times over the entire agar surface, rotating the plate 90 degrees each time. Then, UV-treated material samples were placed on top and incubated at 37 $^{\circ}\text{C}$ for 20 h. The size of the annular inhibition zones free of bacterial growth was determined using ImageJ software (ImageJ 1.53t). The test was conducted in triplicate.

Antimicrobial activity suspension test. Material samples were cut and sterilized under UV light as described in the “Disc diffusion assay” section. The concentration of the overnight bacterial cultures of *E. coli* and *S. aureus* in LB broth was adjusted with fresh Mueller–Hinton broth (MHB) to around 7×10^5 colony-forming units (CFU) mL^{-1} . UV-treated samples were put in Eppendorf tubes, and 100 μL of pre-heated to 37 $^{\circ}\text{C}$ sterile MHB and 100 μL of working bacterial suspension were added. The pure bacterial suspension was used as a positive control, while pure MHB was used as a negative control. After 4 hours of incubation, the medium from each well was withdrawn, and the samples were washed twice with 400 μL of sterile PBS with gentle vortexing. Primary and washing media were collected together and serially diluted in 96-well plates, and each dilution was plated on LB agar in 3 technical repetitions. The plates were then incubated at 37 $^{\circ}\text{C}$ overnight. Bacterial colonies were counted to estimate cell survival after contact with the materials. The test was conducted in triplicate. Additionally, each treatment suspension was diluted 10^2

more times, spread evenly on LB agar plates at 100 μ l, and incubated at 37 °C overnight.

Evaluation of biocompatibility

Hemocompatibility. A hemolytic assay was performed to determine the blood compatibility of all the prepared samples. Extracts were determined from 8 mg of each type of sample placed in a 2 mL tube. Samples were immersed in 2 mL of PBS, kept at 37 °C, and gently stirred for 24 h. The hemolytic potentials of 100% (non-diluted) extracts and serially diluted (50% and 25%) extracts of 2D_{neat}, 2D_{OCT}, and 3D_{OCT@Ag} were measured according to an earlier report.³⁴ Briefly, healthy fresh human blood was collected using Vacuette tubes containing sodium citrate as an anticoagulant (9 mL; Greiner Bio-One, Frickenhausen, Germany). The procedure was approved by the Local Ethics Committee of the Medical University of Białystok (Permit No. R-I-002/193/2019). 5 mL of whole blood was added to 10 mL of PBS. Then, the red blood cells (RBCs) were isolated from plasma by centrifuging at 500g for 10 min and washed five times with 10 mL of PBS. The obtained RBCs were diluted in PBS to a final volume of 50 mL for further use. For the hemolysis test, 0.2 mL of the diluted RBC suspension (around 5×10^8 cells per mL) was added to 0.8 mL of 100% (non-diluted) extracts and serially diluted (50% and 25%) extracts. The RBC suspension dispersed in PBS was selected as a negative control, and the RBC suspension dispersed in distilled water was used as a positive control. All the suspensions were centrifuged at 10 000g for 3 min after being incubated at 37 °C for 3 h. The absorbance of the resulting supernatant was measured at 540 nm using a microplate reader (Synergy HTX, BioTek, Winooski, VT, USA). The hemolysis rate was calculated according to the following equation:

$$\begin{aligned} \text{Percent hemolysis} = & (\text{sample absorbance} \\ & - \text{negative control absorbance}) \\ & / (\text{positive control absorbance} \\ & - \text{negative control absorbance}) \times 100 \end{aligned} \quad (4)$$

Cytotoxicity. Cytotoxicity tests were carried out using the L929 line of fibroblasts (Sigma Aldrich). Cells were cultivated in a 75 cm² flask in a medium consisting of high glucose Dulbecco's modified Eagle's medium (DMEM), 10% fetal bovine serum (FBS), and 1% antibiotics. Cells were incubated in a 5% CO₂ environment at 37 °C. For cell detachment from the flask, cells were washed in PBS. Then 5 mL of 0.05% trypsin solution was added to the cells, and the flask with cells was placed in the incubator for a few minutes. After obtaining the harvested cells, 10 ml of culture medium was added and centrifuged. The centrifugation was carried out at an ambient temperature. The pellet was resuspended with a culture medium to obtain the required cell density. Different studies were performed to determine the cellular response to 2D membranes and 3D scaffolds, including cytotoxicity on extracts and cellular morphology.

Cellular viability. Extracts for *in vitro* tests were determined from 8 mg of each type of sample placed in a 24-well plate

according to the procedure reported before.³⁵ Briefly, samples were immersed in 2 ml of culture medium per well, maintained at 37 °C, and gently stirred for 24 h. For reference, wells with and without samples were filled with the medium. At the same time, L929 cell suspension was seeded into another 48-well plate in the same amount of wells as sample extracts plus control with a density of 1.5×10^4 cells per well and put in an incubator for 24 h. Then, the culture medium from cell-seeded wells was replaced with 100% (non-diluted) extracts and serially diluted (50% and 25%) extracts of 2D_{neat}, 2D_{OCT}, and 3D_{OCT@Ag} samples. After that, the plate was placed in the incubator for another 24 h.

In the next step, extracts were removed, and each well was filled with 180 mL of PBS and 20 mL of Presto blue reagent. After this step, the plate was returned to the incubator for 60 min. This step was completed, and 100 mL from each well was transferred to the 96-well plate. The fluorescence read with excitation/emission 530/620 nm filters was measured using 530/620 nm excitation/emission wavelength using a Fluorescent Accent FL from Thermo Fisher Scientific. The results were compared with the Presto Blue fluorescence of blank samples, which did not show metabolic activity, and the control (tissue culture plate, TCP), which showed 100% viability. The cellular number was determined based on studies on extracts and calibration curves. Briefly, the calibration curve was prepared after 3 days of cell cultivation on TCP based on the known number of cells: 2.5, 5, 10, and 20×10^3 determined with a TC20 automated cell counter (Bio-Rad) and relative fluorescence unit (RFU) determined (Fluorescent Accent FL Thermo Fisher Scientific) from Presto Blue for this known number of cells.³⁵

Fibroblast morphology. The verification of cellular morphology after contact with 25% of extracts was carried out by fluorescence microscopy. L929 cells were seeded with a density of 20×10^4 per well in 400 mL of the 48-well plate medium, and after 24 h, the medium was replaced with extracts. After 24 h of cultivation, cells were fixed in 3% formaldehyde for 20 min and then kept in 0.01% Triton $\times 100$ for 5 min to permeabilize cell membranes. Then, cellular nuclei and cytoskeleton were stained for 30 min in a mixed solution of ActinGreen and NucBlue, whose molecules bind to the cytoskeleton and nucleus DNA, respectively. Images were taken with a Leica AM TIRF MC in magnifications of 100 \times and 400 \times .

Statistics

Statistics were used to evaluate the statistical significance between data from drug release, surface wettability, and biological studies. The results of DSC, WAXS, drug release, and biological studies are presented as the mean value \pm SD. The statistical analyses were conducted for $p < 0.05$ using the GraphPad Prism 8.0.1 software. Two-way ANOVA in Tukey's multiple comparisons was performed as required. The p below 0.05 was considered to be significant statistically, where $0.05 > p > 0.01$ is assigned as "**", $0.01 > p > 0.001$ is set as "***", and $p < 0.001$ is assigned as "****".

Results and discussion

Preparation of 2D_{OCT} and 3D_{OCT@Ag} scaffolds

It is well known that the properties of nanofibers, like layer thickness, porosity, morphology, dimensions, and resulting functionalities, can be easily tailored according to the need by material selection, manipulating the electrospinning parameters, and post-spinning treatments.^{36–39} Among them, post-spinning of fibrous membranes is a valuable technique for fabricating innovative nanoplateforms with on-demand features. In the present study, we used post-modification to transform a drug-loaded 2D nanofiber membrane into a 3D scaffold and to decorate the fiber surface with Ag NPs simultaneously. A critical aspect for co-loading of antibacterial cargos in/on 3D nanofiber scaffolds is the drug's ability to be released from the carrier at the physiological temperature and not during the fabrication process, *i.e.*, at room temperature. Our previous research has studied the preparation of the bioresponsive nanofibers with a well-tuned T_g for a controlled drug release from fibers at 37 °C, and this method was used to prepare OCT-loaded electrospun nanofiber membrane to avoid the loss of drug. The process associated with the simultaneous fabrication of drug-eluting 3D nanofiber scaffolds decorated with *in situ* reduced Ag NPs is shown in Fig. 1. During the post-processing, the AgNO₃ solution would penetrate the 2D mat, resulting in a uniformly Ag NP-decorated and 3D nanofibrous scaffold when reacting with sodium borohydride.²⁸ However, due to its hydrophobic nature, the 2D_{neat} membrane could not absorb aqueous AgNO₃ solution. This characteristic not only led to inhibited filling of the next sodium borohydride solution into the nano/micropores of the membrane but also a failure of *in situ* assemblies of Ag NPs on nanofibers. As a result, gas formation *in situ* in the pores and subsequent pore nucleation was not possible.¹⁶ In other words, the membrane maintained the 2D and unmodified surface structures (Fig. 1a). A similar observation has been made by poly(ϵ -caprolactone) (PCL) and polyvinylidene fluoride (PVDF) as hydrophobic or non-polar polymers,

could not be processed into a 3D architecture using aqueous sodium borohydride solution.¹⁶

Being a cationic surfactant and antimicrobial agent, OCT not only changed the wetting behavior of the 2D membrane from hydrophobic to hydrophilic but also endowed the nanofibers with antibacterial properties, enabling it to be modified into a multifunctional 3D scaffold in a “one stone, two birds” manner. When 2D_{OCT} replaced 2D_{neat}, the AgNO₃ solution was rapidly diffused through the outer layers towards the core of the superhydrophilic membrane driven by the capillary effect. Remarkably, as can be seen from the photograph (Fig. 1b), the color of the 2D_{OCT} membrane pre-immersed in AgNO₃ solution turned from white to deep brown upon treatment with an aqueous sodium borohydride medium, indicating the successful *in situ* synthesis of Ag NPs. At the same time, the membrane was gradually transformed into the 3D scaffold with a low-density, macroporous sponge structure. The thickness of the 3D_{OCT@AgNPs} scaffold increased from 0.8 mm to 18 mm after treatment in the medium, and more expansion was achieved by drying in a vacuum oven (Fig. 1c). It is due to the surrounding pressure of the scaffolds being decreased. Consequently, the volume of the gas trapped in those pores increased, further increasing the volume of the nanofibrous scaffolds.¹⁶

Furthermore, SEM images confirmed the scaffold's high porosity and multilayered structure and its nanofiber surface decoration with Ag NPs. As shown in the cross-sectional image (Fig. 2a and d), the 2D nanofibrous membrane was composed of tightly packed fiber layers with superficially planar pores. In contrast, the 3D_{OCT@AgNPs} scaffolds were characterized by suitable interconnected porous structures with average pore sizes ranging from approximately 300 to 900 μm . From the SEM micrograph taken at a higher magnification (Fig. 2f), supported Ag NPs were observed to be distributed uniformly and with a relatively lower coverage density on the fiber surface of the 3D scaffold. A more careful inspection revealed that these nanosized silver particles with a narrow size distribution were found to be firmly attached to the fiber surfaces.

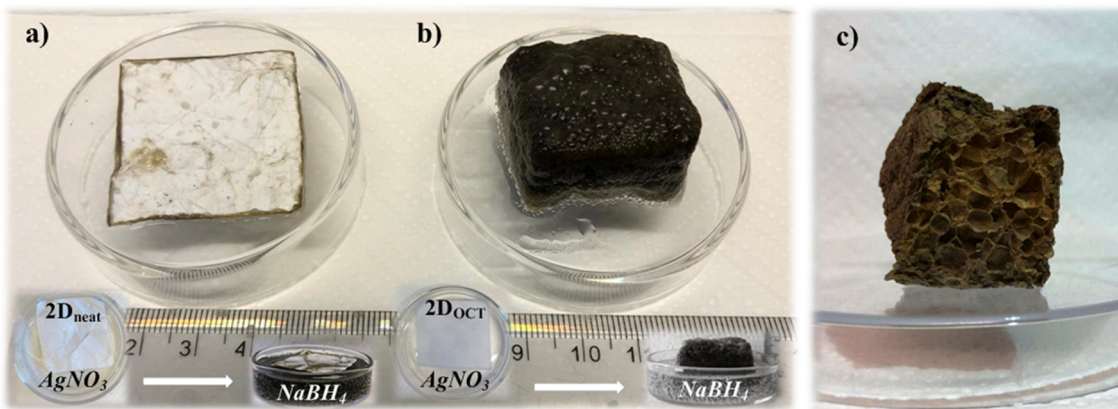


Fig. 1 Representative photographs of the samples treated with subsequent immersion medium (a) 2D_{neat}, (b) 2D_{OCT}, and (c) digital image of the cross-section of 3D_{OCT@Ag}.

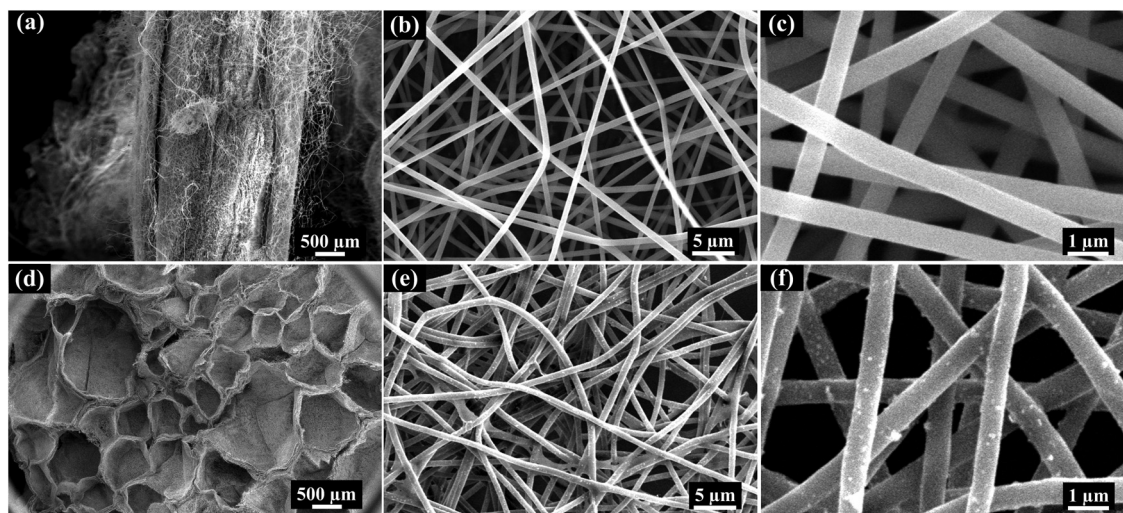


Fig. 2 Morphology of samples via SEM images: (a) a cross-section of the 2D_{OCT} membrane, (b and c) its images with different magnifications, (d) a cross-section of the 3D_{OCT}@AgNPs scaffold, and (e and f) its images with different magnifications.

Based on the morphological analysis, aqueous sodium borohydride medium was employed as a reducing agent for Ag NPs synthesis and used as the producer of hydrogen gas, which can lead to a dramatic change in the morphology and dimensions of 2D_{OCT} membranes.

Analysis of hydrophilic/hydrophobic behavior

The water contact angle test for electrospun membranes with and without OCT and the scaffold was measured to investigate the scaffold's wettability properties (Fig. 3). During 3 minutes, the contact angle value does not differ considerably from the 2D_{neat} specimen, essentially representing the hydrophobicity of the PMMA/ERS fibers ($133.60^\circ \pm 1.3$). This result revealed that the 2D_{neat} electrospun fibers have hydrophobic properties. On the other hand, the water contact angle considerably decreased after adding OCT, even though PMMA and OCT are

intrinsically hydrophobic components. Blended PMMA/ERS led to the highest contact angle, and adding OCT to the polymer blend decreased the contact angle significantly to $25.97^\circ \pm 6.4$ at 0.13 seconds. Fig. 3a depicts that the contact angle of the 3D_{OCT}@Ag scaffold enhanced dramatically, and the drop disappeared immediately at 0.01 seconds. After adding OCT, both 2D_{OCT} and 3D_{OCT}@Ag samples turned into superhydrophilic scaffolds. As OCT is a surfactant, the OCT's structure likely makes it more Gemini surfactant-like properties.⁴⁰ This Gemini surfactant has a short hydrophobic spacer on all sides and a long hydrophilic spacer in the middle.⁴¹ It seems that after adding OCT/HFIP combination to the polymer solution, these two hydrophobic sides of OCT were changed from the polymeric matrix structure. Therefore, this superhydrophilicity property is caused by two cationic active centers.⁴²

Nanofibers with tunable wettability by adding anionic, non-ionic, and cationic surfactants have been reported by thorough investigations in the literature.^{43–45} For instance, Kurusu *et al.*⁴⁵ observed the incorporation of the nonionic amphiphilic surfactant, Pluronic, which contains hydrophobic poly(propylene oxide) as the midblock and hydrophilic poly(ethylene oxide) as the end-blocks, into hydrophobic electrospun nanofibers resulted in superhydrophilic membrane. The idea was that the hydrophobic segment would help anchor the molecule to the polymer matrix while hydrophilic segments would be active at the surface when in contact with water.⁴³

Chemical and phase composition of samples

Based on the WAXS analysis, the structure of raw material (OCT), 2D_{neat}, and 2D_{OCT}, and 3D scaffold, was determined and is shown in Fig. 4a. In the case of OCT, many diffraction peaks result from the crystalline structure of this substance. Otherwise, in the case of polymers, there is a broad halo from the amorphous phase registered as the only one for the 2D_{neat}

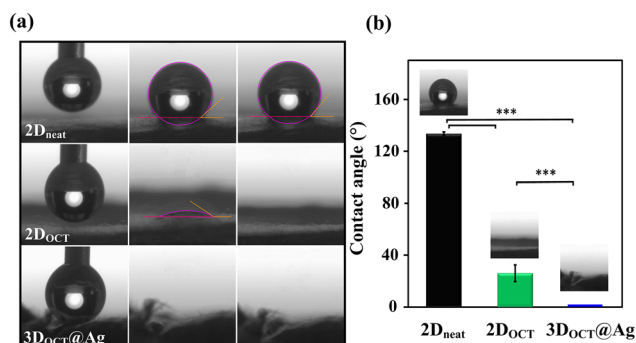


Fig. 3 (a) Contact angles with optical pictures with different times: 0 s (left column), 0.01 s (middle column), 2.5 min (right column), and (b) the bar chart of contact angle measurement at 0.01 s. Statistical analysis was performed between the contact angle of 2D_{neat} vs. 2D_{OCT} and 3D_{OCT}@Ag. Significance represented as *** = 0.0001 to 0.001, extremely significant.

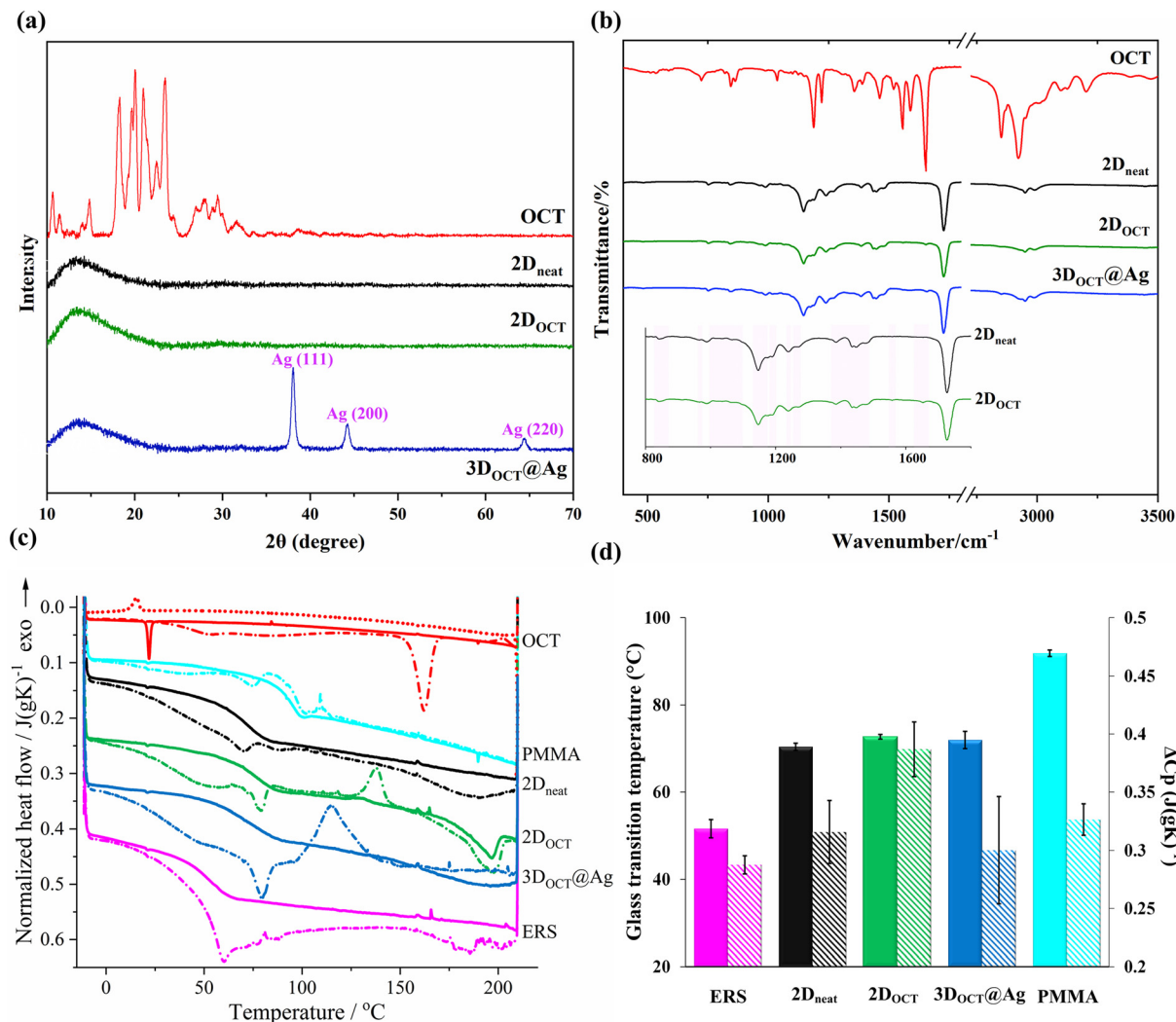


Fig. 4 (a) WAXS patterns and (b) FT-IR spectra of raw OCT, 2D nanofibrous membranes, and 3D scaffold. (c) DSC first heating scans (short dashed-dotted lines), second heating scans (solid lines) registered for the fiber mats (pure PMMA, pure ERS), their blend ($2D_{neat}$), the blend with the addition of OCT ($2D_{OCT}$), for the scaffold ($3D_{OCT@Ag}$) as well as for pure OCT, for which also a cooling scan (short dot line) is shown; for clarity sake, the curves were shifted; moreover, the pure OCT scans were multiplied by a factor of 0.3. (d) Glass transition temperature, T_g , and enthalpy change at T_g , ΔC_p , with standard deviation as determined from the second heating scans registered for five samples.

and $2D_{OCT}$ fibers. As expected, the peaks located at 38.06° , 44.27° , and 64.32° , which could be assigned to the (1 1 1), (2 0 0), and (2 2 0) crystallographic planes of the face-centered cubic Ag crystal structure, were found for the $3D_{OCT@Ag}$ nanofiber scaffolds, confirming the assembly of Ag NPs.⁴⁶ The fact that for the OCT-loaded nanofibrous membrane, there is only an amorphous halo can be explained by complete payload dispersion within the blended polymers. Similarly, the rapid evaporation of solvent induced by the electrospinning process prevents the organization of drug molecules into crystalline lattices and leads to complete amorphization.⁴⁷

Infrared spectroscopy was utilized to characterize the molecular nature and to confirm the OCT and Ag encapsulation in the samples (Fig. 4b). A prominent absorption peak of the OCT range at $600\text{--}800\text{ cm}^{-1}$ and $1000\text{--}1350\text{ cm}^{-1}$ was allocated to the C-X and aromatic C-N of OCT, respectively.

Furthermore, the peak ranges of OCT at $1640\text{--}1690\text{ cm}^{-1}$ and $3100\text{--}3500\text{ cm}^{-1}$ were recorded for the C=N aromatic and N-H stretching.⁴⁸ To confirm OCT encapsulation in the electrospun fibers, an aromatic C=N signal of OCT appeared at 1653 cm^{-1} of $2D_{OCT}$; however, it was not observed in the $2D_{neat}$ membrane.³⁰ Another difference between $2D_{OCT}$ and $2D_{neat}$ is shown by the pink highlights on the bottom of the primary FTIR spectrum. These changing and shifting values of the peaks are indicated as the main changes in the chemical and physical properties of both samples (inset of Fig. 4b). As far as Ag NPs do not have absorption in the FTIR curves,⁴⁶ the similar FTIR spectrum of samples except for the shifting bands was noticeable. Besides, this marginally shifted toward a lower value, and the peak at 2936 cm^{-1} is related to the asymmetric CH_2 stretching band after synthesizing the Ag NPs. These results indicated the successful synthesis of the Ag NPs.

DSC results and analysis

DSC analysis was performed to determine the miscibility of the polymeric components and the effects of the addition of OCT and Ag NPs on the glass transition and other thermal behaviors. The heat flow registered during the first heating scans showed many thermal artifact effects located below and within the expected glass transition making the determination of the T_g for fabricated samples difficult (the short dash lines in Fig. 4c). This is probably due to the fibrous/membrane morphology, the presence of mechanical stress and/or solvent residue, which are released. Moreover, exclusively for the blends, the addition of OCT resulted in the appearance of exothermic (100–150 °C) and endothermic (170–210 °C) peaks, which are not present in heating and cooling scans for pure OCT. The respective peaks may result from crystallization and melting occurring in the PMMA/ERS blend induced by the presence of OCT molecules.

The glass transition temperatures (T_g) were determined from the second heating scans, which are presented in Fig. 4c as solid lines. It is evident that the heating scans always show a single glass transition indicating total blend miscibility. The T_g depends on the blend composition and presence of OCT and Ag NPs. The results are presented in Fig. 4d. It may be seen that for pure ERS, T_g is at 51 °C, for pure PMMA at 92 °C, and in between for their blend, at *ca.* 70 °C. The addition of OCT increases only slightly the T_g to *ca.* 72 °C, and there is no effect of Ag NP addition in the case of the 3D scaffold. As regards the enthalpy change (ΔC_p), the lowest value is found for pure ERS, 0.287 J (g K)⁻¹, for pure PMMA 0.326 J (g K)⁻¹, and for their blend 0.316 J (g K)⁻¹. The addition of OCT increases ΔC_p evidently to almost 0.4 J (g K)⁻¹, while adding Ag NPs in the case of the 3D scaffold reduces it back to 0.3 J (g K)⁻¹ (Fig. 4d).

Drug loading and encapsulation efficiency of the 2D membrane and 3D scaffold

The loading content and encapsulation efficiency of OCT from the nanofibers were studied, and for the 2D nanofiber membrane they were similar to the theoretical concentration (3% w/w in solid state) (Table 1). The high encapsulation efficiency of OCT is due to its non-volatile nature as well as high solubility in the composite polymer solution. On the other hand, a significant decrease in the encapsulation efficiency was observed from the 3D_{OCT@Ag} scaffold, which implies there was a loss of OCT during the transformation of the 2D nanofiber membrane into the 3D scaffold by subsequent immersion in the aqueous solution.

Table 1 Drug (OCT) loading content and drug encapsulation efficiency in the 2D membrane and 3D scaffold. Data are expressed as a mean \pm standard deviation ($n = 3$)

Samples	Loading content \pm SD (%)	Encapsulation efficiency \pm SD (%)
2D _{OCT}	2.75 \pm 0.14	91.88 \pm 3.98
3D _{OCT@Ag}	2.09 \pm 0.17	69.66 \pm 5.04

In vitro drug release

The cumulative release of the drug from the 2D_{OCT} membrane and 3D_{OCT@Ag} scaffold was quantified in PBS buffer at 25 °C, 32 °C, and 37 °C, respectively, to assess the effect of temperature on OCT release. As shown in Fig. 5a, biphasic release can be distinguished in the release profiles; after the first 4 hours of rapid release, the following time interval showed sustained release of OCT from the 2D sample up to 144 h at 32 °C and 37 °C. It is well known that the surface wettability of electrospun fibers has a significant effect on the release behavior of their loaded drugs.⁴⁹ Hence, the initial rapid-release phase can be mainly related to the hydrophilicity of the 2D_{OCT} membrane. Moreover, the membrane also exhibited temperature-dependent drug release trends. At 25 °C and 32 °C, the OCT release was suppressed, and the release rate decreased after 24 h. The accumulated release amounts were less than 33% and 41% after 144 h. As the temperature increases, the drug release rate accelerates drastically. The accumulated release of OCT was determined to be 79.16 \pm 2.86% at 37 °C by the same release time. These results suggested that the 2D membranes with optimized T_g can be used as the precursor nanofibers to retain the loaded drugs during the post-processing of the 2D membrane at room temperature; thus, the 3D scaffold provides a controlled delivery at body temperature.

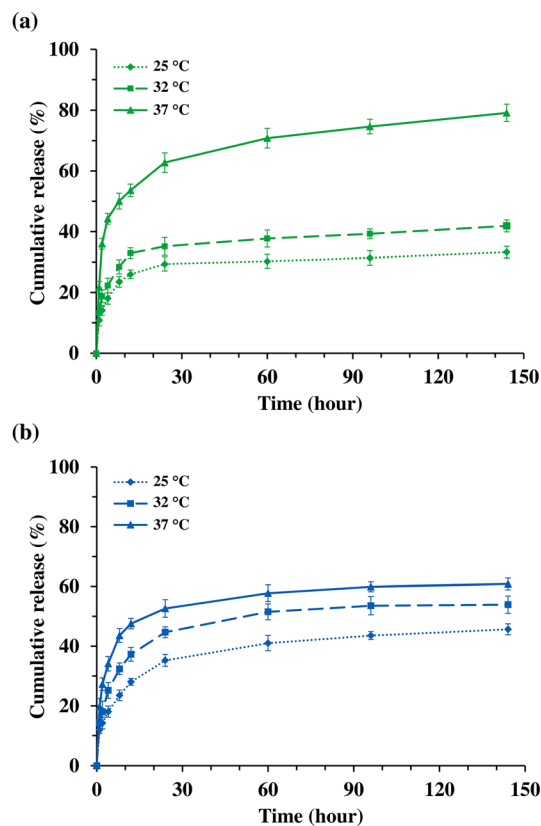


Fig. 5 Cumulative OCT *in vitro* release from the (a) 2D_{OCT} membrane and (b) 3D_{OCT@Ag} scaffold at three different temperatures (25 °C, 32 °C, and 37 °C).

In the case of the 3D_{OCT}@Ag scaffold, a similar biphasic release trend was noted at all temperatures (Fig. 5b). Regarding the different temperatures used for the release test, the change between 25 °C and 37 °C had a tiny effect on the OCT release profiles. At 37 °C, the OCT release from scaffold 3D_{OCT}@Ag was slightly lower than its counterpart, the 2D_{OCT} membrane; however, it is expected that this is not significant in terms of its antibacterial properties due to the combination with Ag NPs. The little difference in OCT release was probably due to the decreased encapsulation efficiency. Considering the acquired results, a multifunctional 3D nanofibrous scaffold that shows burst biphasic drug release characteristics may be advantageous for application on the infected wound, where an immediate effect is necessary. In addition, it is expected to have another advantage that of being easily attached to the infected wound as compared to other wound dressings due to the presence of cationic ERS polymer,⁵⁰ and it provides a simple clinical translation.

Ag content and Ag release profile

As the synergistic antibacterial property of the 3D_{OCT}@Ag scaffold is due to the release of silver elements from the nanoparticles, its actual amount and release study were conducted. ICP-MS measurements revealed that the amount of silver species in the sample was 5.45 wt% (based on the actual weight of the scaffold). Moreover, the silver release kinetic displayed an initial burst effect, and then a gradual and prolonged silver release was observed (Fig. 6). After 144 h of reaction, the 3D_{OCT}@Ag scaffold consequently lost only 2.25% (data not shown) of its silver, indicating good aqueous stability of Ag NPs. In other words, a successful chemical interaction occurred between the decorated Ag NPs and the nanofibrous scaffold during *in situ* synthesis.⁵¹

Antibacterial activity analysis

The antibacterial activity of the materials was determined using a disc diffusion assay and bacterial suspension test against *E. coli* (Gram-negative) and *S. aureus* (Gram-positive), two typical

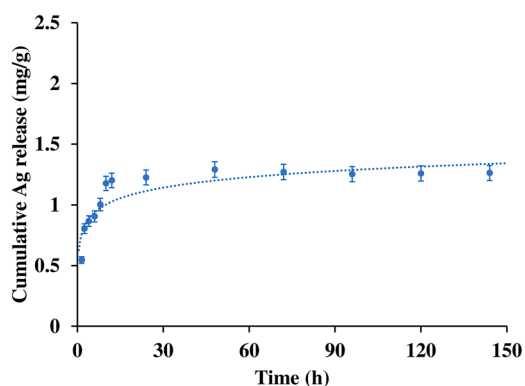


Fig. 6 Ag release profile from the 3D_{OCT}@Ag scaffold determined by ICP-MS analysis.

microorganisms associated with wound infections.⁵² The inhibition zones appeared around both drug-loaded materials, reaching significantly higher values around the 3D_{OCT}@Ag scaffold; they were, however, minimal around 2D_{OCT} on *E. coli* (Fig. 7a and b). This clearly indicated greater antibacterial activity of Ag NPs-decorated 3D scaffold compared to 2D_{OCT} membrane against both strains. The zones around the 3D_{OCT}@Ag scaffold were of equal size in both microorganisms. No inhibition zones appeared around the 2D_{neat} membrane neither on *S. aureus*, nor *E. coli* inoculated plates.

In the bacterial suspension test, both of the drug-loaded materials proved to be effective against both of the microorganisms after just 4 hours of contact time, showing a detection limit 5-log reduction compared to the CFU ml⁻¹ of the bacterial cells in positive controls and in contact with 2D_{neat} membranes, where the growth was unhindered (Fig. 7c and d). In contrast to the equally extraordinary performance of both drug-loaded materials against the selected strains in the suspension test, the difference in the antimicrobial efficacy of the 3D_{OCT}@Ag scaffold compared to that of 2D_{OCT} shown in the disc diffusion test results might be important when considering different moisture levels in an infected wound, where diffusion might be locally hindered, thus favoring the 3D_{OCT}@Ag scaffold. The advantage of the 3D_{OCT}@Ag scaffold over 2D_{OCT} was undoubtedly caused by Ag ion activity, as OCT release from this material was of an even slightly lower rate than from 2D_{OCT} at the physiological temperature.

Two antimicrobial agents have been responsible for the results – OCT, dispersed in the polymer matrix of the nanofibers, and silver (Ag), in the form of NPs decorating their surface. OCT induces rapid cell death by disrupting their lipid barrier, acting in a detergent-like manner.^{53,54} The antibacterial mode of action of Ag results from the generation of reactive oxygen species, blocking expression of proteins supporting bacterial life, disruption of the membrane permeability, and mutations of the bacterial genome, leading to bacterial cell death.^{55,56} The wish to increase the time of antibacterial activity of silver resulted in the vast development of silver NPs, as the gradual release of silver from Ag NPs allows a sustained antibacterial effect, uninterrupted by silver precipitation.⁵⁵ While OCT acts against various microorganisms, including drug-resistant isolates, silver ions activity is narrowed to Gram-negatives due to Gram-positive's thick cell wall.^{54,55} Previous studies on Ag NPs reported, however, that these are, in turn, more effective against Gram-positives than Gram-negatives.^{57,58} Besides acting as a simple Ag ions reservoir, Ag NPs possess a unique ability to penetrate bacterial membranes, followed by ion release inside the cells.^{55,59} Thanks to a synergistic effect of OCT and Ag NPs, there was no difference in the antibacterial performance of 3D_{OCT}@Ag material samples against Gram-positive and Gram-negative strains in our study (Fig. 7a and c).

Biocompatibility analysis

***In vitro* hemocompatibility results.** The fundamental requirement of new material that directly contacts the wound is that it must be a blood-biocompatible and non-cytotoxic

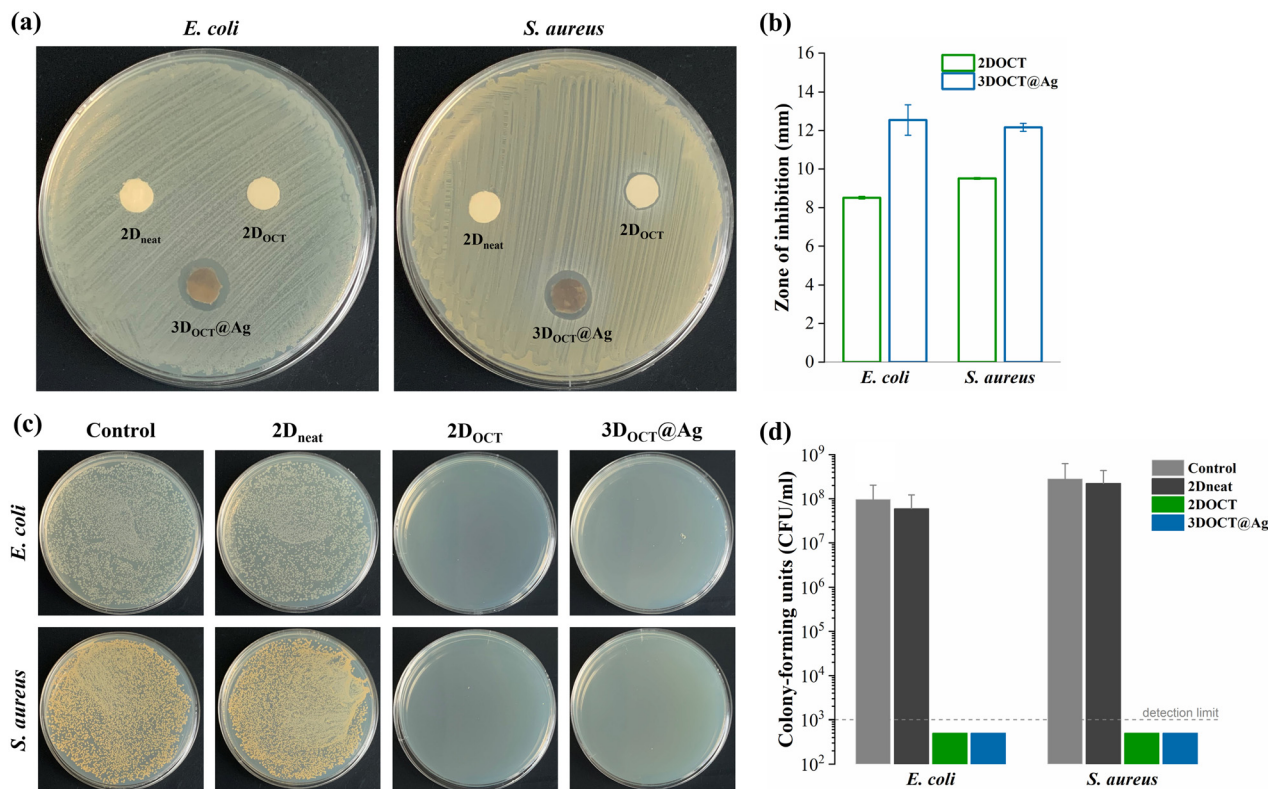


Fig. 7 Disc diffusion assay against *E. coli* DH5 α and *S. aureus* ACCT 6538 (a and b): one of 3 representative experiments shown (a); quantitative evaluation of inhibition zones around drug-loaded materials on *E. coli* and *S. aureus* (b) ($n = 3$), data are expressed as a mean with a standard deviation. Antibacterial activity of the materials against suspensions of *E. coli* DH5 α and *S. aureus* ACCT 6538 (c and d): bacteria after treatment with 2D_{OCT}, 3D_{OCT@Ag}, and 2D_{neat} materials and without the treatment (c); the number of colony-forming units (CFU) ml⁻¹ after 4 h of incubation with tested materials (d) ($n = 3$), data are expressed as a mean with a standard deviation. For graphic reasons, data points below the detection limit (10³ CFU ml⁻¹) were set to 0.5 \times 10³ CFU ml⁻¹.

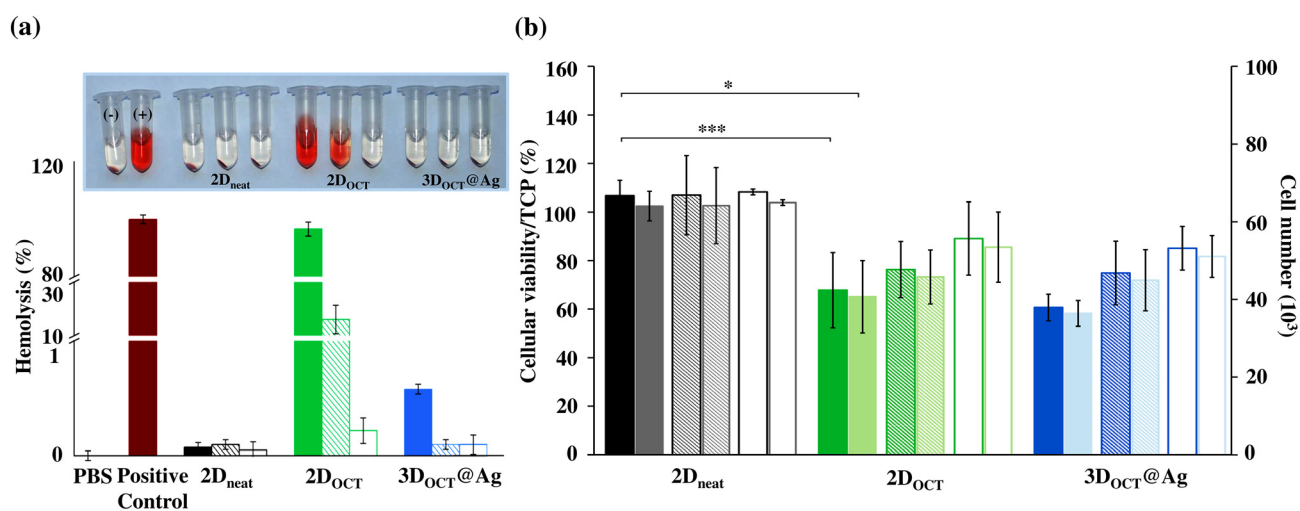


Fig. 8 (a) Hemolysis ratios of human RBCs treated with extracts of 2D_{neat}, 2D_{OCT}, and 3D_{OCT@Ag}: 100% (filled), 50% extracts, (patterned), and 25% (non-filled) extracts in comparison to control. Insert images of the tube containing RBCs solution show direct observation of hemolysis. The red solution indicates that the RBCs were destroyed and hemoglobin was released. (-) represents negative control, and (+) represents positive control. Data are expressed as a mean with a standard deviation. (b) Cellular viability and number after 24 h in contact with extracts of 2D_{neat}, 2D_{OCT}, and 3D_{OCT@Ag}: 100% (filled), 50% extracts, (patterned), and 25% (non-filled) extracts in comparison to control TCP (tissue culture plastic). Data are expressed as a mean with a standard deviation. Statistical analysis was performed between cells after contact with the extract of 2D_{neat} vs. 2D_{OCT} and 3D_{OCT@Ag}. Significance represented as * = 0.01 to 0.05, significant; ** = 0.001 to 0.01 very significant; *** = 0.0001 to 0.001, extremely significant.

character. According to ISO 10993-4, hemolysis tests should be done to describe blood compatibility. Hemolysis is the rupturing of erythrocytes and the release of their contents into the plasma. The hemolytic potential of 100% (non-diluted) extracts and serially diluted (50% and 25%) extracts of 2D_{neat}, 2D_{OCT}, and 3D_{OCT@Ag} were investigated, and the results were presented in Fig. 8a. The hemolytic percentage of 2D_{neat} sample has been observed as below 2%, which is in agreement to ISO 10994-requirements and this material is blood-compatible. No hemolytic rates were detected for 2D_{OCT} membrane only in extraction 25%, probably due to the higher amount of drug release. However, the 3D_{OCT@Ag} scaffold showed dramatically different results in comparison to its counterpart from 2D_{OCT}. Considering the same amount of OCT molecules loaded in both samples, the decreased hemolysis at the 3D_{OCT@Ag} scaffold is very likely caused by OCT loss during the transformation of the 2D nanofiber membrane into the 3D scaffold. Furthermore, it was reported that scaffolds containing Ag NPs had a lower hemolysis effect on human RBC than the scaffold, which had no nanoparticles.⁶⁰ Their study was supportive of our results, and it can therefore be concluded that the 3D_{OCT@Ag} scaffold is blood compatible and could be used as wound dressings.

In vitro cytotoxicity assay results. According to rules described in International Organization for Standardization (ISO) 10993-1, Biological Evaluation of Medical Devices – Part 1: Evaluation and Testing within a Risk Management Process, one of the main essential aspects is noncytotoxic character. Therefore, cytotoxicity was determined on L929 fibroblasts by Presto Blue assay in contact with the extracts of 2D_{neat}, 2D_{OCT}, and 3D_{OCT@Ag} compared to TCP after 24 h (Fig. 8b). Extracts of 2D_{neat} indicated higher cellular viability than 2D_{OCT} membrane and 3D_{OCT@Ag} scaffold. All 25% and 50% extracts were noncytotoxic for cells, and the viability was higher than 70% of TCP. Two-way ANOVA in Tukey's multiple comparisons of 2D_{neat} and 2D_{OCT}, 2D_{neat}, and 3D_{OCT@Ag} depicted significance at non-diluted extracts (100%) ($p < 0.001$) and 50% extract ($p = 0.017 > 0.01$). Additionally, the cell number determined according to sufficient methodology is in agreement with the Presto blue test (Fig. 9).

L929 fibroblasts are a type of eukaryotic, adherent, connective cell line in a living tissue responsible for producing an extracellular matrix, and a fibrous environment is their natural habitat.⁶¹ After 24 h of cultivation, the fibroblast's amount and shape in contact with extracts of 2D_{neat}, 2D_{OCT}, and 3D_{OCT@Ag} samples were similar to that in the control, which corresponds with cellular viability (Fig. 9). Cells indicated a morphology similar to the morphology of cells seeded on TCP (Fig. 9). They are well-spread and exhibit good intercellular interactions. Cells extend their filopodia and lamellipodia to attach themselves to the surface, which is characteristic of enhanced cell-material interaction.

Regarding the presence of antimicrobial agents such as antibiotics, anti-inflammatory drugs, and inorganic NPs in the delivery system, the concentration-dependent reduction in cell viability has been reported in prior studies.^{62–64} Van Meurs *et al.* found that OCT concentration below 2×10^{-3} mg mL⁻¹

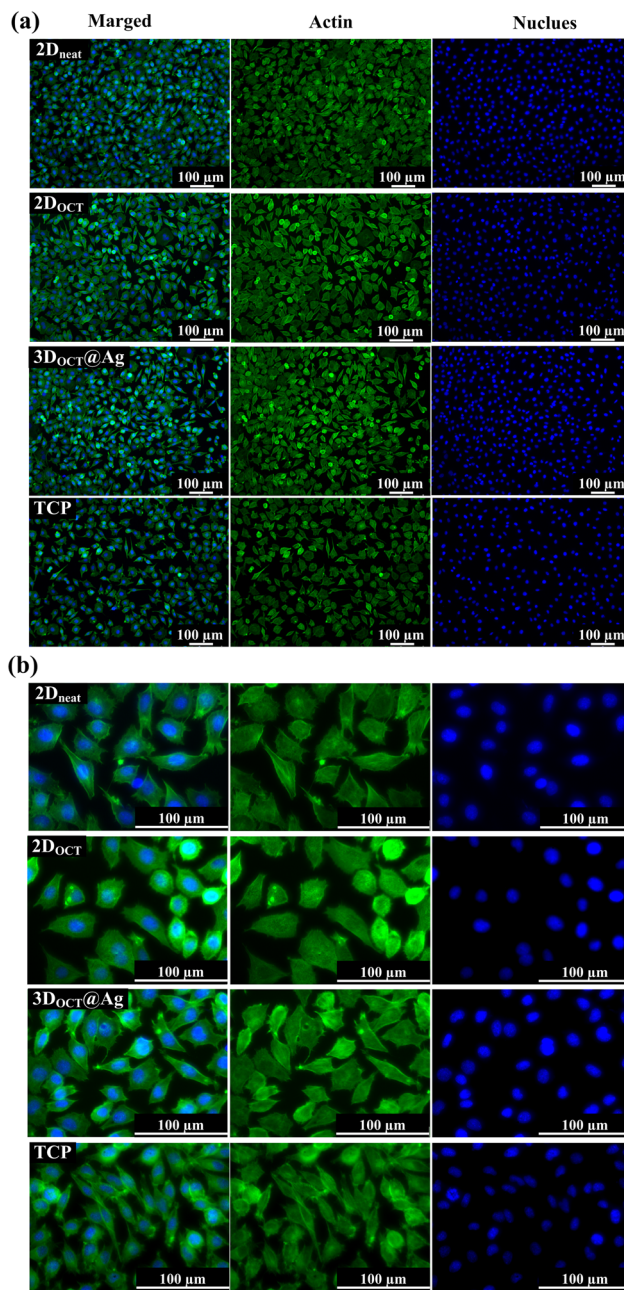


Fig. 9 L929 cells cultured for 24 h in contact with samples extracts in comparison with TCP as a control: cellular nucleus in blue (right column), actin skeleton on green (middle column), merged nucleus and actin images (left column), (a) magnification 100 \times , (b) magnification 400 \times .

does not affect cellular viability,⁶⁵ while Klaue *et al.* decreased this amount to 5×10^{-4} mg mL⁻¹ and confirmed the ability to provide significant antimicrobial activity at the same concentration.⁶⁶ Our 100% extracts exhibited much higher OCT concentration (1.2×10^{-2} mg mL⁻¹). However, as reported, this value might be decreased in the subsequent investigations without losing microbial activity. Bearing in mind the results of the antibacterial activity of 3D scaffolds against *E. coli*

(Gram-negative) and *S. aureus* (Gram-positive), eukaryotic cell viability and their morphology *in vitro*, it is expected that the developed 3D scaffolds will promote diabetic wound healing and skin repair *in vivo*.

Conclusions

In summary, we have simply fabricated a multilayered macroporous 3D scaffold based on drug-eluting nanofibers. Nanofiber membranes with different surface wetting behaviors (hydrophobic 2D_{neat} and hydrophilic 2D_{OCT}) were subjected to post-processing treatment to functionalize the scaffold. Due to the encapsulation of OCT, the hydrophilic-modified 2D_{OCT} membrane led to the successful fabrication of drug-eluting 3D nanofiber scaffolds decorated with Ag NPs by sodium borohydride treatment. SEM revealed the *in situ* assembly of Ag NPs on the surface of nanofibers, and what is more, Ag NPs were distributed without aggregation on the nanofibers. The fabricated 3D scaffold exhibits a biphasic release behavior consisting of initial fast release, followed by sustained release, and this characteristic may be advantageous for application on the infected wound, where an immediate effect is necessary. Moreover, the difference in the antimicrobial efficacy of the 3D_{OCT}@Ag scaffold compared to 2D_{OCT} shown in the disc diffusion test results might be important when considering different moisture levels in an infected wound, where diffusion might be hindered, thus favoring the 3D_{OCT}@Ag scaffold. The *in vitro* cell viability assay indicates the biocompatibility of the multifunctional 3D nanofiber scaffold, particularly when encapsulating a low concentration of OCT in the 2D membranes. In conclusion, this scaffold would be promising and suitable for diabetic wound healing and skin repair.

Ethics statement

The procedure of blood collection was approved by the Local Ethics Committee of the Medical University of Białystok (Permit No. R-I-002/193/2019); informed consents were obtained from human participants.

Author contributions

Altangerel Amarjargal: Conceptualization, methodology, analysis, investigation, writing – original draft, writing – review and editing, and supervision. Zahra Moazzami Goudarzi: Analysis, investigation, and writing – review and editing. Olga Cegielska: Analysis, investigation, and writing – review and editing. Arkadiusz Gradys: Analysis, investigation, and writing – review and editing. Dorota Kolbuk: Analysis, investigation, and writing – review and editing. Bartłomiej Kalaska: Analysis, investigation, and writing – review and editing. Anna Ruszczyńska: Analysis, investigation, and writing – review and editing. Paweł Sajkiewicz: Writing – review and editing and funding acquisition.

Conflicts of interest

There are no conflicts to declare.

Acknowledgements

A. Amarjargal gratefully acknowledges the Polish National Agency for Academic Exchange (NAWA) through the Ulam Programme (agreement number PPN/ULM/2020/1/00056/U) for the financial support of her stay at the Institute of Fundamental Technological Research, Polish Academy of Sciences.

References

- 1 S. Asghari, Z. Rezaei and M. Mahmoudifard, *Analyst*, 2020, **145**, 2854–2872.
- 2 D. M. dos Santos, D. S. Correa, E. S. Medeiros, J. E. Oliveira and L. H. C. Mattoso, *ACS Appl. Mater. Interfaces*, 2020, **12**, 45673–45701.
- 3 Z. Yin, L. Sun, L. Shi, H. Nie, J. Dai and C. Zhang, *Biomater. Sci.*, 2022, **10**, 753–769.
- 4 Z. Sheng, Y. Xu, Z. Tong, Z. Mao and Y. Zheng, *Colloid Interface Sci. Commun.*, 2022, **48**, 100620.
- 5 S. J. Lee, H. Nah, W. K. Ko, D. Lee, H. J. Moon, J. S. Lee, M. Heo, Y. S. Hwang, J. B. Bang, S. H. An, D. N. Heo and I. K. Kwon, *ACS Omega*, 2021, **6**, 28307–28315.
- 6 Z. Zhu, Y. Liu, Y. Xue, X. Cheng, W. Zhao, J. Wang, R. He, Q. Wan and X. Pei, *ACS Appl. Mater. Interfaces*, 2019, **11**, 36141–36153.
- 7 M. A. Mohamady Hussein, E. Guler, E. Rayaman, M. E. Cam, A. Sahin, M. Grinholc, D. Sezgin Mansuroglu, Y. M. Sahin, O. Gunduz, M. Muhammed, I. M. El-Sherbiny and M. Megahed, *Carbohydr. Polym.*, 2021, **270**, 118373.
- 8 T. S. Sampath Kumar and V. Yogeshwar Chakrapani, in *Advances in Experimental Medicine and Biology*, Springer New York LLC, 2018, vol. 1078, pp. 29–47.
- 9 Q. Zhao, J. Wang, H. Cui, H. Chen, Y. Wang, X. Du, Q. Zhao, J. Wang, H. Cui, H. Chen, Y. Wang and X. Du, *Adv. Funct. Mater.*, 2018, **28**, 1801027.
- 10 A. Z. Unal and J. L. West, *Bioconjugate Chem.*, 2020, **31**, 2253–2271.
- 11 J. Li, T. Zhang, M. Pan, F. Xue, F. Lv, Q. Ke and H. Xu, *J. Nanobiotechnol.*, 2022, **20**, 1–18.
- 12 S. Chen, J. V. John, A. McCarthy and J. Xie, *J. Mater. Chem. B*, 2020, **8**, 3733–3746.
- 13 J. Y. Song, H. il Ryu, J. M. Lee, S. Hwan Bae, J. W. Lee, C. C. Yi and S. M. Park, *Nanoscale Res. Lett.*, 2021, **16**, 116.
- 14 T. Wang, Y. Zhai, M. Nuzzo, X. Yang, Y. Yang and X. Zhang, *Biomaterials*, 2018, **182**, 279–288.
- 15 D. Ahirwal, A. Hébraud, R. Kádár, M. Wilhelm and G. Schlatter, *Soft Matter*, 2013, **9**, 3164–3172.
- 16 M. K. Joshi, H. R. Pant, A. P. Tiwari, H. J. Kim, C. H. Park and C. S. Kim, *Chem. Eng. J.*, 2015, **275**, 79–88.

- 17 J. Jiang, S. Chen, H. Wang, M. A. Carlson, A. F. Gombart and J. Xie, *Acta Biomater.*, 2018, **68**, 237–248.
- 18 K. Zhang, X. Bai, Z. Yuan, X. Cao, X. Jiao, Y. Li, Y. Qin, Y. Wen and X. Zhang, *Biomaterials*, 2019, **204**, 70–79.
- 19 F. Dehghani and N. Annabi, *Curr. Opin. Biotechnol.*, 2011, **22**, 661–666.
- 20 Y. Chen, Z. Jia, M. Shafiq, X. Xie, X. Xiao, R. Castro, J. Rodrigues, J. Wu, G. Zhou and X. Mo, *Colloids Surf., B*, 2021, **201**, 111637.
- 21 Q. Gao, H. Gu, P. Zhao, C. Zhang, M. Cao, J. Fu and Y. He, *Mater. Des.*, 2018, **157**, 159–169.
- 22 S. Chen, H. Wang, A. McCarthy, Z. Yan, H. Joon Kim, M. A. Carlson, Y. Xia and J. Xie, *Nano Lett.*, 2019, **19**, 2059–2065.
- 23 C. Deraedt, L. Salmon, S. Gatard, R. Ciganda, R. Hernandez, M. Mayor and D. Astruc, *Chem. Commun.*, 2014, **50**, 14194–14196.
- 24 S. C. Jung, Y. K. Park, H. Y. Jung and S. C. Kim, *J. Nanosci. Nanotechnol.*, 2017, **17**, 2833–2836.
- 25 K. J. Carroll, D. M. Hudgins, S. Spurgeon, K. M. Kemner, B. Mishra, M. I. Boyanov, L. W. Brown III, M. L. Taheri and E. E. Carpenter, *Chem. Mater.*, 2010, **22**, 6291–6296.
- 26 P. Nakielski, S. Pawłowska, C. Rinoldi, Y. Ziai, L. de Sio, O. Urbanek, K. Zembrzycki, M. Pruchniewski, M. Lanzi, E. Salatelli, A. Calogero, T. A. Kowalewski, A. L. Yarin and F. Pierini, *ACS Appl. Mater. Interfaces*, 2020, **12**, 54328–54342.
- 27 Y. Zhang, M. Zhang, D. Cheng, S. Xu, C. Du, L. Xie and W. Zhao, *Biomater. Sci.*, 2022, **10**, 1423–1447.
- 28 J. Y. Moon, J. Lee, T. I. Hwang, C. H. Park and C. S. Kim, *Carbohydr. Polym.*, 2021, **273**, 118603.
- 29 A. Amarjargal, M. Brunelli, G. Fortunato, F. Spano, C. S. Kim and R. M. Rossi, *J. Drug Delivery Sci. Technol.*, 2019, **52**, 8–14.
- 30 F. Pan, A. Amarjargal, S. Altenried, M. Liu, F. Zuber, Z. Zeng, R. M. Rossi, K. Maniura-Weber and Q. Ren, *ACS Appl. Bio Mater.*, 2021, **4**, 4271–4279.
- 31 Ch. N. Patra, R. Priya, S. Swain, G. Kumar Jena, K. C. Panigrahi and D. Ghose, *Future J. Pharm. Sci.*, 2017, **3**, 33–45.
- 32 O. Cegielska, M. Sierakowski, P. Sajkiewicz, K. Lorenz and K. Kogermann, *Eur. J. Pharm. Biopharm.*, 2022, **180**, 48–62.
- 33 C. F. Rediguieri, R. C. Sassonia, K. Dua, I. S. Kikuchi and T. de Jesus Andreoli Pinto, *Eur. Polym. J.*, 2016, **82**, 181–195.
- 34 C. He, Z. Q. Shi, L. Ma, C. Cheng, C. X. Nie, M. Zhou and C. S. Zhao, *J. Mater. Chem. B*, 2014, **3**, 592–602.
- 35 B. Niemczyk-Soczynska, A. Gradys, D. Kolbuk, A. Krzton-Maziopa, P. Rogujski, L. Stanaszek, B. Lukomska and P. Sajkiewicz, *RSC Adv.*, 2022, **12**, 26882–26894.
- 36 M. A. Alfaro De Prá, R. M. Ribeiro-do-Valle, M. Maraschin and B. Veleirinho, *Mater. Lett.*, 2017, **193**, 154–157.
- 37 X. Xie, D. Li, Y. Chen, Y. Shen, F. Yu, W. Wang, Z. Yuan, Y. Morsi, J. Wu and X. Mo, *Adv. Healthc. Mater.*, 2021, **10**, 2100918.
- 38 A. Amarjargal, L. D. Tijing, C. H. Park, I. T. Im and C. S. Kim, *Eur. Polym. J.*, 2013, **49**, 3796–3805.
- 39 S. Tabakoglu, D. Kolbuk and P. Sajkiewicz, *Biomater. Sci.*, 2022, **11**, 37–61.
- 40 A. N. Vereshchagin, N. A. Frolov, V. Y. Konyuhova, E. A. Kapelistaya, K. A. Hansford and M. P. Egorov, *RSC Adv.*, 2021, **11**, 3429–3438.
- 41 C. A. Stewart, Y. Finer and B. D. Hatton, *Sci. Rep.*, 2018, **8**, 1–12.
- 42 A. Flodin, Master's thesis, Chalmers University of Technology, 2019.
- 43 J. H. Lee, Y. M. Ju and D. M. Kim, *Biomaterials*, 2000, **21**, 683–691.
- 44 R. Beigmoradi, A. Samimi and D. Mohebbi-Kalhari, *Polym. Test.*, 2021, **93**, 106970.
- 45 R. S. Kurusu and N. R. Demarquette, *Langmuir*, 2015, **31**, 5495–5503.
- 46 A. Amarjargal, L. D. Tijing, H. K. Shon, C. H. Park and C. S. Kim, *Appl. Surf. Sci.*, 2014, **308**, 396–401.
- 47 H. Bukhary, G. R. Williams and M. Orlu, *Int. J. Pharm.*, 2018, **549**, 446–455.
- 48 R. J. Lohar, V. M. Patil, V. C. Yeligar and S. S. Patil, *World J. Pharm. Pharm. Sci.*, 2016, **5**, 1697–1701.
- 49 G. Kuang, Z. Zhang, S. Liu, D. Zhou, X. Lu, X. Jing and Y. Huang, *Biomater. Sci.*, 2018, **6**, 324–331.
- 50 P. D. S. Chaves, L. A. Frank, A. G. Frank, A. R. Pohlmann, S. S. Guterres and R. C. R. Beck, *AAPS PharmSciTech*, 2018, **19**, 1637–1646.
- 51 S. Radhakrishnan, S. Nagarajan, H. Belaid, C. Farha, I. Iatsunskyi, E. Coy, L. Soussan, V. Huon, J. Bares, K. Belkacemi, C. Teyssier, S. Balme, P. Miele, D. Cornu, N. Kalkura, V. Cavailles and M. Bechelany, *Mater. Sci. Eng., C*, 2021, **118**, 111525.
- 52 L. J. Bessa, P. Fazii, M. di Giulio and L. Cellini, *Int. Wound J.*, 2015, **12**, 47–52.
- 53 N. Malanovic, A. Ön, G. Pabst, A. Zellner and K. Lohner, *Int. J. Antimicrob. Agents*, 2020, **56**, 106146.
- 54 N. Malanovic, J. A. Buttress, D. Vejzovic, A. Ön, P. Pillar, D. Kolb, K. Lohner and H. Strahl, *Appl. Environ. Microbiol.*, 2022, **8**, 1–15.
- 55 V. Pareek, R. Gupta and J. Panwar, *Mater. Sci. Eng., C*, 2018, **90**, 739–749.
- 56 S. Nakamura, M. Sato, Y. Sato, N. Ando, T. Takayama, M. Fujita and M. Ishihara, *Int. J. Mol. Sci.*, 2019, **20**, 3620.
- 57 D. A. Mosselhy, M. A. El-Aziz, M. Hanna, M. A. Ahmed, M. M. Husien and Q. Feng, *J. Nanopart. Res.*, 2015, **17**, 1–10.
- 58 K. H. Cho, J. E. Park, T. Osaka and S. G. Park, *Electrochim. Acta*, 2005, **51**, 956–960.
- 59 J. S. McQuillan, H. Groenaga Infante, E. Stokes and A. M. Shaw, *Nanotoxicology*, 2012, **6**, 857–866.
- 60 M. Bagheri, M. Validi, A. Gholipour, P. Makvandi and E. Sharifi, *Bioeng. Transl. Med.*, 2022, **7**, e10254.
- 61 J. Dulnik, O. Jeznach and P. Sajkiewicz, *J. Funct. Biomater.*, 2022, **13**, 272.
- 62 M. F. Sanchez, M. L. Guzman, J. Flores-Martín, M. C. Del Puerto, C. Laino, E. A. Soria, A. C. Donadio, S. Genti-Raimondi and M. E. Olivera, *Sci. Rep.*, 2022, **12**, 16035.

- 63 M. Bagheri, M. Validi, A. Gholipour, P. Makvandi and E. Sharifi, *Bioeng. Transl. Med.*, 2022, **7**, e10254.
- 64 W. Purnamasari, T. A. Budiastanti, A. Aminatun, U. Rahmah, S. Sumarsih, J. Y. Chang and M. Z. Fahmi, *RSC Adv.*, 2022, **12**, 8019–8029.
- 65 S. J. van Meurs, D. Gawlitta, K. A. Heemstra, R. W. Poolman, H. C. Vogely and M. C. Kruyt, *J. Bone Jt. Surg.*, 2014, **96**, 285–291.
- 66 A. Klaue, M. Maraldi, C. Piviali, D. Moscatelli and M. Morbidelli, *Eur. Polym. J.*, 2020, **138**, 109987.